

pubs.acs.org/JACS Communication

# Colloidal Synthesis of Monodisperse High-Entropy Spinel Oxide Nanocrystals

Jonathan L. Rowell, Minsoo Kang, Dasol Yoon, Kevin Zhijian Jiang, Yafu Jia, Héctor D. Abruña, David A. Muller, and Richard D. Robinson\*



Cite This: J. Am. Chem. Soc. 2024, 146, 17613-17617



**ACCESS** I

III Metrics & More

Article Recommendations

SI Supporting Information

**ABSTRACT:** Synthesis of high-entropy oxide (HEO) nanocrystals has focused on increasing the temperature in the entropy term  $(T(\Delta S))$  to overcome the enthalpy term. However, these high temperatures lead to large, polydisperse nanocrystals. In this work, we leverage the low solubility product  $(K_{\rm sp})$  of metal oxides and optimize the Lewis-acid-catalyzed esterification reaction for equal rate production of the cation monomers to synthesize HEO nanocrystals at low temperatures, producing the smallest (<4 nm) and most monodisperse (<15% size dispersity) HEOs to date. We apply these HEO nanocrystals as electrocatalysts, exhibiting promising activity toward the oxygen evolution reaction in alkaline media, with an overpotential of 345 mV at 10 mA/cm<sup>2</sup>.

## ■ INTRODUCTION

High-entropy oxide (HEO) nanomaterials have gained significant interest in numerous fields for their enhanced performance and stability. 1-3 The number of studies on spinel HEOs is limited;<sup>4-7</sup> only one approach reports small (<10 nm) nanocrystals, albeit with considerable size variation. Colloidal synthesis techniques, involving the decomposition of precursors within an organic ligand matrix, can produce the highest quality nanocrystals with the lowest size dispersity and solution stability without agglomeration.8 However, no studies have utilized colloidal synthesis techniques for the preparation of HEO nanocrystals. This paucity of colloidal methodology is likely due to the prevailing assumption that achieving a highentropy phase necessitates high temperatures and/or pressures to increase the  $T(\Delta S)$  term in the Gibbs free energy equation. But, working under these extreme conditions leads to uncontrolled nanocrystal growth. Based on a previous lowtemperature solution-based synthesis of spinel HEOs,5 we theorized that high temperatures may not be essential/ necessary for forming HEO phases. We hypothesized that leveraging the solubility product  $(K_{sp})$  can overcome thermodynamic constraints from lattice strain, forming multimetal phases without an increased entropic driving force. To test this hypothesis we modified literature procedures where metal carboxylates are reacted with alcohols to produce metal hydroxides (metal oxide monomers) via an esterification pathway (Table S1). 9-12 Assuming the Lewis acid character of the metal centers is the major factor determining esterification and thus precursor decomposition rate, we hypothesized that achieving HEO nanocrystals should be possible by choosing metals with similar electronegativities.

We synthesized HEO spinels by modifying the cations that occupy the tetrahedral (A) and octahedral [B] interstitial sites of the spinel lattice. Utilizing an  $Fe_3O_4$  magnetite scaffold, our objective was to engineer HEO spinels, accommodating either divalent (2+) or trivalent (3+) cations at the A or B sites,

contingent on the level of inversion in the lattice.<sup>13</sup> Our objective for the HEO sample with 3+ cations (HEO-3+) was to synthesize spinels with equimolar ratios of Al, Sc, Fe, Ga, and In, while the 2+ cation in this sample consisted of Co and Fe. In the 2+ cation HEO samples (HEO-2+) the goal was to synthesize spinels with equimolar ratios of 2+ cations including Mn, Fe, Co, Ni, and Zn.

Low-resolution transmission electron microscopy (TEM) images of the 3+ spinel HEOs showed faceted, small nanocrystals that average 4.1 nm in diameter with a small size dispersity (Figure 1a). The powder X-ray diffraction (PXRD) (Figure 1b) pattern of the HEO-3+ correlates to magnetite but shifted to lower two theta due to the large ionic radii of substituted cations like indium. The shift is significant, averaging 1.3% lattice expansion over the three peaks sampled (Table S2). Elemental levels determined by inductively coupled plasma mass spectrometry (ICP-MS) reveal the composition to be 20.7% Fe, 29.5% Co, 11.3% Al, 9.8% Ga, 18.5% In, and 10.2% Sc (Figure 1c and Table S3), well above the 5% threshold to qualify as a high-entropy material. 1,14 Xray photoelectron spectroscopy (XPS) measurements corroborated the composition (Figure 1c). XPS analysis indicates all elements exhibit a 3+ oxidation state, except for Fe and Co, which also display a 2+ oxidation state (Figures 1d and S1). Energy dispersive X-ray spectroscopy (EDS) mapping in a scanning transmission electron microscope (STEM) shows that each particle contains all six elements (Figure 1e-j). The distribution of cations within each nanocrystal is somewhat heterogeneous, with Co and Fe appearing more localized in the

Received: April 6, 2024 Revised: May 31, 2024 Accepted: June 3, 2024 Published: June 17, 2024





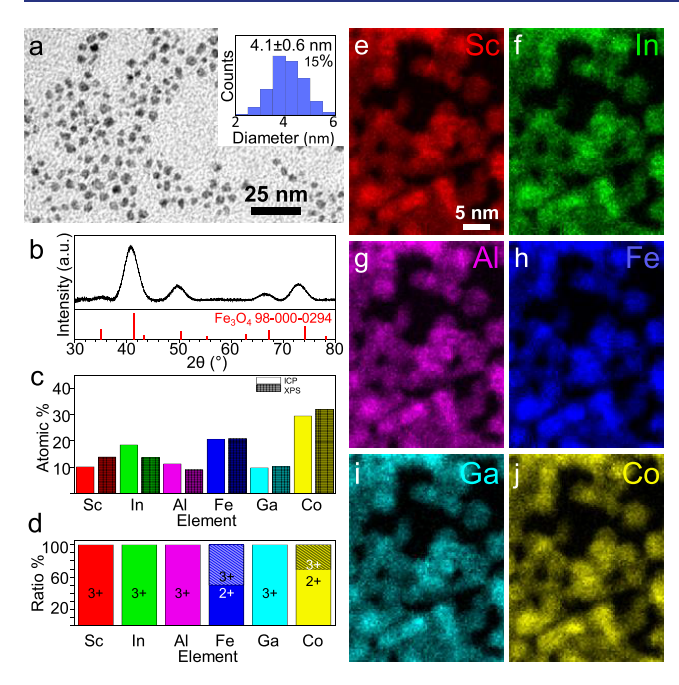


**Figure 1.** 3+ cation high-entropy spinel nanocrystals (HEO-3+). (a) TEM and size distribution of 4.1 nm nanocrystals with 15% dispersity. (b) PXRD pattern matches the magnetite spectrum but shifted to smaller  $2\theta$  values. (c) Elemental composition via ICP-MS (plain) and XPS (checkered). (d) Oxidation state data from XPS. (e–j) Energy dispersive X-ray spectroscopy (EDS) elemental mapping.

core, whereas other elements, like Sc, appear more concentrated on the periphery (Figure S2).

High-angle annular dark field STEM (HAADF-STEM) images reveal single crystals with a spinel structure (Figure 2). When viewed down the [110] direction, the HAADF-STEM image and its fast Fourier transform (FFT) align with the kinematic electron diffraction simulation of single-crystal magnetite (Figure 2a-e). While in this orientation, the atomic columns exhibit mostly uniform brightness for the cations, when viewing the lattice down [111] (Figure 2f,g) there is noticeable heterogeneity in the brightness of the columns. This alternation of atomic column intensities indicates the systematic incorporation of the high-entropy mixture into the spinel B sites. When observing the particle along [110], the HAADF intensity is unable to distinguish between the distribution of light and heavy 3+ cations. This is because each column contains many atoms (~10 atoms in the particle center) and, thus, statistically exhibits a random mix of both types of cations. However, when viewed from [111], certain atomic columns (Figure 2h, green columns) contain only 1-3 B-site cations. Of these columns, some appear brighter, indicating heavier elements such as indium, while others appear darker in intensity, indicating higher occupation of lighter elements like aluminum. This disparity in intensity occurs because intensity scales roughly as the square  $(Z^{1.7})$  of the atomic number. This finding implies the cation mixture is preferentially occupying the B sites.

For the HEO-2+ samples, larger-sized nanocrystals were 3.9 nm with a 15% size dispersity (Figure 3a), and smaller-sized HEO-2+ nanocrystals were 3.1 nm with only a 13% size dispersity (Figure 3k). Both HEO-2+ samples had PXRD patterns that matched magnetite (Figure 3b,l). The 2+ samples had little shift from the magnetite values due to the similarity in the ionic radii of the 2+ cations. HAADF-STEM imaging

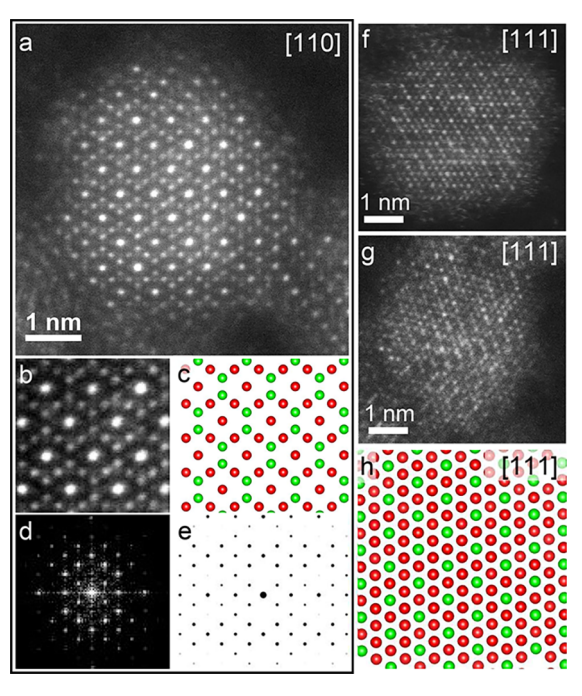


**Figure 2.** HAADF-STEM image of HEO-3+ nanocrystals. (a) Highresolution HAADF-STEM image viewed down the [110] zone. (b) Magnified image from (a). (c) Model of the magnetite [110]. (d) FFT taken at the center of the nanocrystal in (a). (e) Kinematic electron diffraction simulation of single-crystal magnetite. (f, g) Highresolution HAADF-STEM images viewed down the [111] zone. (h) The corresponding [111] zone model.

displayed a single-crystal spinel nanocrystal viewed down the [100] direction (Figure 3c). EDS mapping of the larger HEO-2+ sample indicates that each particle contains all five elements, although Zn and Mn appear at lower concentrations (Figure 3d–i). ICP-OES indicates that all elements are found in the sample with 5.4% Co, 7.6% Ni, 3.9% Zn, and 1.7% Mn, with XPS corroborating these results (Figure 3j and Table S4). In the smaller HEO-2+ samples, the composition of 2+ precursor cations is higher, with Mn, Co, Zn, and Ni at 6.6%, 6.8%, 7.4%, and 7.3%, respectively (Figure 3m and Table S4), which exceeds the 5% threshold. <sup>1,14</sup>

The electrochemical response of spinel HEO/Ketjen Black composites in 1.0 M KOH shows a typical capacitive-type response of high surface area carbon with broad peaks at lower potentials (Figure 4a), with the amplitude being higher in the case of the HEO-2+ samples than the HEO-3+ samples. This difference is likely due to surface cations of the HEO-2+ sample (Mn, Fe, Co, Ni) being more redox active (Table S5) and being present in both the 2+ and 3+ oxidation states (Figure S3). Most of the cations in the HEO-3+ sample (Al, Ga, In, Sc) have no redox activity due to their preference for the 3+ oxidation state 16 (d10 or d0 electron counts). Both HEOs show promising/favorable overpotentials for the oxygen evolution reaction (OER): 345 and 355 mV at 10 mA/cm<sup>2</sup> for the HEO-2+ and HEO-3+, respectively (Figure 4b). These overpotentials exceed the performance by Wang et al. for a spinel HEO,5 which had an overpotential of 400 mV, improving to 350 mV only after combining with carbon nanotubes. Binary, ternary, and multimetal oxide (MMO) particles prepared by similar methods (Figures S4-S8) have lower OER activity than the HEO samples (Figures 4b and S9, Table S10). Also tested were  $Mn_{0.07}Co_{0.23}Ni_{0.21}Fe_{2.49}O_4$ 

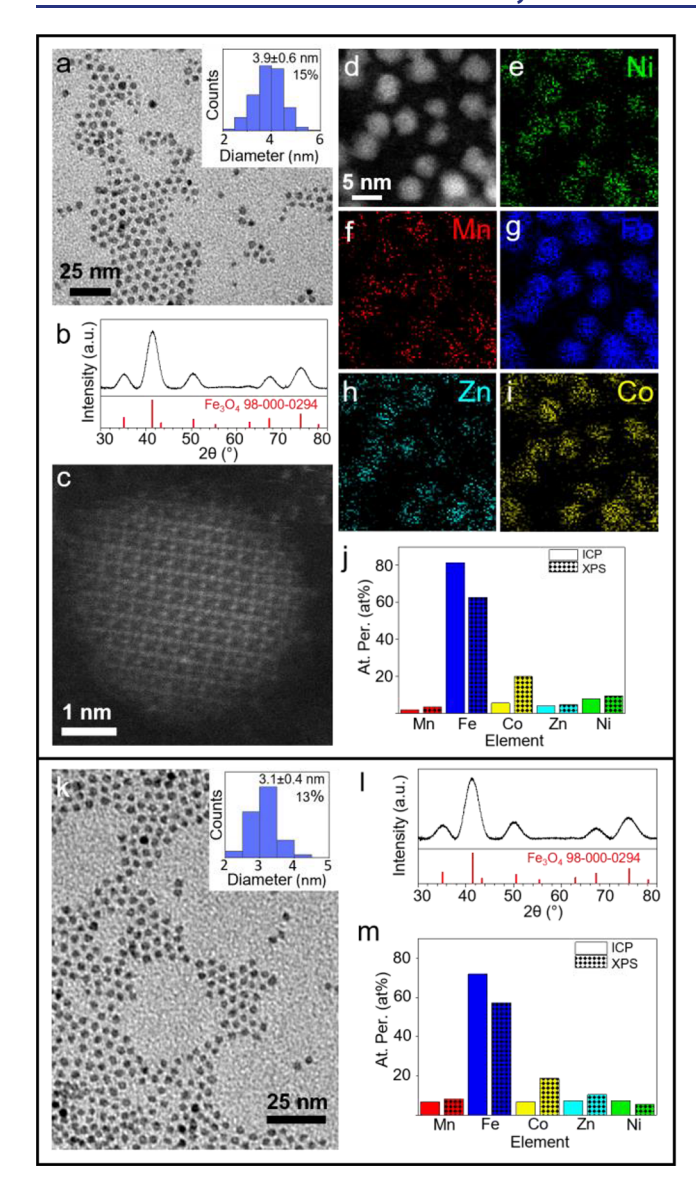


**Figure 3.** Characterization of HEO-2+ nanocrystals. (a–j)  $\sim$ 4 nm HEO-2+ nanocrystals. (a) TEM and size distribution showing 3.9  $\pm$  0.6 nm particles (15% dispersity). (b) PXRD follows the magnetite spectrum. (c) HAADF-STEM showing lattice fringes that match the [100] spinel direction. (d–i) EDS elemental mapping. (j) Elemental composition via ICP-OES (left, solid) and XPS (right, checkered). (k–m)  $\sim$ 3 nm HEO-2+ nanocrystals. (k) TEM and size distribution showing 3.1  $\pm$  0.4 nm particles (13% dispersity). (l) PXRD follows the magnetite spectrum. (m) Elemental composition via ICP-OES (left, solid) and XPS (right, checkered).

(MMO2) and  $Mn_{0.09}Co_{0.23}Ni_{0.29}Fe_{2.40}O_4$  (MMO3); both had higher overpotentials (Figure S9). Over five voltammetric cycles, the HEO-3+, MMO1, MMO2, MMO3, and binary/ternary ferrite oxide composites shift to higher overpotentials, likely indicating unfavorable restructuring of the catalyst (Figures 4b and S9). The HEO-2+ composite, in contrast, did not shift significantly over five cycles.

Most methods of obtaining HEOs employ high temperatures to increase the value of the  $T(\Delta S)$  term to overcome the enthalpic term in  $\Delta G_{\rm mix} = \Delta H_{\rm mix} - T(\Delta S)$ , where  $\Delta G_{\rm mix}$  is Gibbs free energy of mixing,  $\Delta H_{\rm mix}$  is enthalpy of mixing, T is temperature, and  $\Delta S$  is entropy of mixing (typically unfavorable due to lattice distortion in high-entropy

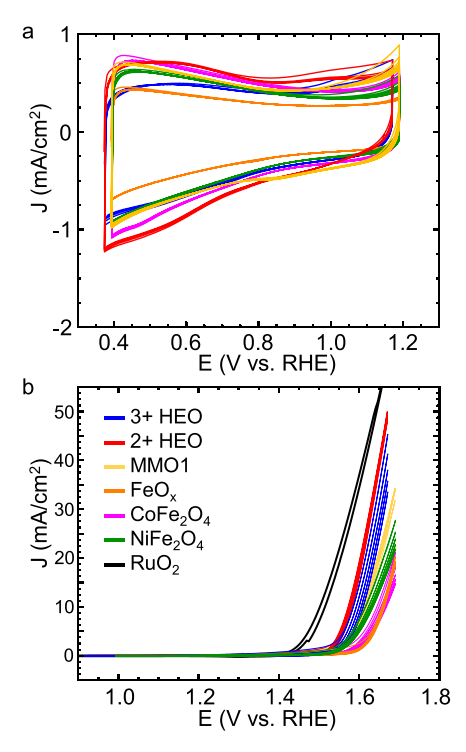


**Figure 4.** Electrochemical characterization of HEOs. Electrolyte was 1.0 M KOH. (a) CV under argon at 50 mV/s. (b) OER polarization curves at 1600 rpm with a 5 mV/s sweep rate. MMO1 composition is  $Co_{0.24}Ni_{0.33}Fe_{2.43}O_4$  by ICP.

materials).<sup>17</sup> But there are precedents for forming HEO nanocrystals at relatively low temperatures.<sup>5,18</sup> We propose that high temperatures are unnecessary due to the low  $K_{\rm sp}$  of oxides.<sup>19,20</sup>

$$Precursor \rightarrow Monomer (irreversible)$$
 (1)

Monomer 
$$\leftrightarrow$$
 Nanocrystal (pseudo-irreversible if  $K_{\rm sp}$  is sufficiently low) (2)

In the normal equilibria that describe the growth of colloids (eqs 1 and 2), the second step (monomer adsorption onto a nanocrystal) is usually described as reversible. But this step is simply the chemical reverse of solubility, and the inverse/ reciprocal of the equilibrium constant is the  $K_{sp}$ . Therefore, if the  $K_{\rm sp}$  of the material is sufficiently low under the reaction conditions, then this second step can be taken as irreversible, and we propose this is the case for spinel oxides. In this case, the rate of the decomposition of the precursors into monomer is the only determinant for cation incorporation. Therefore, if one chooses precursors that all decompose to monomer at similar rates, one can easily achieve a high-entropy oxide phase. We believe that metal-catalyzed esterification is an ideal reaction for this goal. This hypothesis suggests that current use of high temperatures/pressures to form HEOs may be disadvantageous since it confines the period during which each monomer is decomposing, which could increase the degree of elemental clustering in the product (Figure S10).

Metals can act as Lewis acids. They can catalyze esterification of carboxylates while simultaneously producing metal hydroxides, which are monomers of metal oxides (Figure 5). The rate-determining step of esterification under acidic

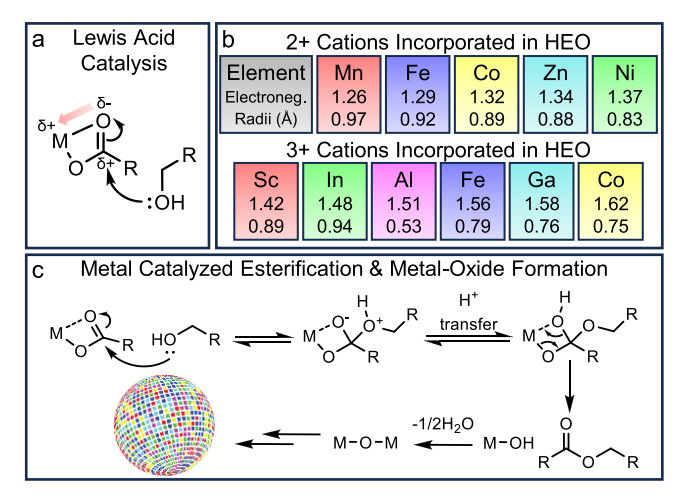


Figure 5. Mechanistic pathway of esterification toward monodisperse colloidal HEO nanocrystals. (a) The Lewis acidity of the metal cation increases the electrophilicity of the carbonyl, lowering activation energy for the tetrahedral intermediate. (b) Cations incorporated; top number is estimated electronegativity; bottom is ionic radii. (c) Esterification mechanism and metal oxide formation pathway.

conditions is often the nucleophilic addition to the carbonyl.<sup>21</sup> Lewis acids can catalyze this step by withdrawing electron density away from the carbonyl carbon, thus increasing electrophilicity (Figure 5a,c). We hypothesized that Lewis acid-catalyzed esterification rates (precursor decomposition; eq 1) will be driven by the Lewis acidity of the cations. Therefore, employing cations with similar electronegativities (Figure 5b and Table S7)<sup>22,23</sup> should be effective in attaining an HEO product. Highly electropositive cations, like Mg, failed to incorporate into the spinel lattice (Figure S11). Additionally, including elements with high reduction potentials, like Cu (Table S5), 16 led to a metallic phase impurity (Figure S12). The arguments on irreversible monomer adsorption imply adding any number of cations will result in an MMO phase, even with fewer than five cations, below the requirement for entropically driven phase stabilization. We synthesized MMOs with only two or three elements besides Fe, using an Fe<sub>3</sub>O<sub>4</sub> scaffold. The results indicate that incorporating a smaller number of additional 2+ cations (Figure S7 and Table S6) is feasible, suggesting multicomponent phase formation need not be entropically stabilized.

# CONCLUSION

We report a novel synthetic methodology toward high-entropy spinel oxide nanocrystals. To our knowledge, this is the first colloidal synthesis of HEO spinels, exhibiting the smallest average particle size and narrowest size dispersity. This result was achieved by recognizing the low  $K_{sp}$  of spinel oxides presents a strong impetus for precipitation, particularly at low reaction temperature. Our finding suggests that other HEO phases and compositions should be accessible, that HEO formation is not necessarily driven by entropic effects, and that any number of cations can be incorporated in spinel nanocrystals, opening the door to a range of uniform-sized multimetal nanocrystals.

#### ASSOCIATED CONTENT

# Supporting Information

The Supporting Information is available free of charge at https://pubs.acs.org/doi/10.1021/jacs.4c04744.

A detailed experimental section, tables of ICP and XPS elemental analysis, EELS elemental mapping of HEO-3+, a table of OER overpotentials, characterization (TEM, XRD, TGA, XPS, ICP) of MMO, binary oxide, ternary oxides, and failed HEOs, XPS (survey and oxidation state) analysis of HEOs, additional electrochemical data for MMO2 and MMO3, and Debeye-Scherrer and other calculations (PDF)

# AUTHOR INFORMATION

### Corresponding Author

Richard D. Robinson - Department of Materials Science and Engineering and Kavli Institute at Cornell for Nanoscale Science, Cornell University, Ithaca, New York 14853, United States; o orcid.org/0000-0002-0385-2925; Email: rdr82@ cornell.edu

#### Authors

Jonathan L. Rowell – Department of Chemistry and Chemical Biology, Cornell University, Ithaca, New York 14853, United States; orcid.org/0000-0002-2959-8638

Minsoo Kang - Department of Materials Science and Engineering, Cornell University, Ithaca, New York 14853, United States

Dasol Yoon - Department of Materials Science and Engineering, Cornell University, Ithaca, New York 14853, *United States*; orcid.org/0000-0003-2284-7010

Kevin Zhijian Jiang – Department of Materials Science and Engineering, Cornell University, Ithaca, New York 14853, United States

Yafu Jia - Department of Materials Science and Engineering, Cornell University, Ithaca, New York 14853, United States

Héctor D. Abruña - Department of Chemistry and Chemical Biology, Cornell University, Ithaca, New York 14853, United States; orcid.org/0000-0002-3948-356X

David A. Muller - School of Applied and Engineering Physics and Kavli Institute at Cornell for Nanoscale Science, Cornell University, Ithaca, New York 14853, United States; orcid.org/0000-0003-4129-0473

Complete contact information is available at: https://pubs.acs.org/10.1021/jacs.4c04744

# **Author Contributions**

All authors have given approval to the final version of the manuscript.

The authors declare no competing financial interest.

# **ACKNOWLEDGMENTS**

Research was primarily supported as part of the Center for Alkaline Based Energy Solutions (CABES), an Energy Frontier Research Center funded by the U.S. Department of Energy (DOE), Office of Science, Basic Energy Sciences (BES), under Award # DE-SC0019445. This work was supported in part by the National Science Foundation (NSF) under Award Nos. DMR-1809429 and CMMI-2120947. This work also made use of the Cornell Center for Materials Research Shared Facilities, which are supported through the NSF MRSEC program (DMR-1719875). The FEI Titan Themis 300 was acquired through NSF-MRI-1429155, with additional support from Cornell University, the Weill Institute, and the Kavli Institute at Cornell. The Thermo Fisher Spectra 300 X-CFEG was

acquired with support from PARADIM, an NSF MIP (DMR-2039380), and Cornell University.

#### REFERENCES

- (1) Tomboc, G. M.; Zhang, X.; Choi, S.; Kim, D.; Lee, L. Y. S.; Lee, K. Stabilization, Characterization, and Electrochemical Applications of High-Entropy Oxides: Critical Assessment of Crystal Phase—Properties Relationship. *Adv. Funct. Mater.* **2022**, 32 (43), No. 2205142.
- (2) Sun, Y.; Dai, S. High-entropy materials for catalysis: A new frontier. Science Advances 2021, 7 (20), No. eabg1600.
- (3) Dey, G. R.; Soliman, S. S.; McCormick, Č. R.; Wood, C. H.; Katzbaer, R. R.; Schaak, R. E. Colloidal Nanoparticles of High Entropy Materials: Capabilities, Challenges, and Opportunities in Synthesis and Characterization. *ACS Nanoscience Au* **2024**, *4*, 3.
- (4) Katzbaer, R. R.; Dos Santos Vieira, F. M.; Dabo, I.; Mao, Z.; Schaak, R. E. Band Gap Narrowing in a High-Entropy Spinel Oxide Semiconductor for Enhanced Oxygen Evolution Catalysis. *J. Am. Chem. Soc.* **2023**, *145*, 6753.
- (5) Wang, D.; Liu, Z.; Du, S.; Zhang, Y.; Li, H.; Xiao, Z.; Chen, W.; Chen, R.; Wang, Y.; Zou, Y.; Wang, S. Low-temperature synthesis of small-sized high-entropy oxides for water oxidation. *J. Mater. Chem. A* **2019**, 7 (42), 24211–24216.
- (6) Wang, G.; Qin, J.; Feng, Y.; Feng, B.; Yang, S.; Wang, Z.; Zhao, Y.; Wei, J. Sol—Gel Synthesis of Spherical Mesoporous High-Entropy Oxides. ACS Appl. Mater. Interfaces 2020, 12 (40), 45155–45164.
- (7) Zhang, Q.; Hu, Y.; Wu, H.; Zhao, X.; Wang, M.; Wang, S.; Feng, R.; Chen, Q.; Song, F.; Chen, M.; Liu, P. Entropy-Stabilized Multicomponent Porous Spinel Nanowires of NiFeXO<sub>4</sub> (X = Fe, Ni, Al, Mo, Co, Cr) for Efficient and Durable Electrocatalytic Oxygen Evolution Reaction in Alkaline Medium. *ACS Nano* **2023**, *17* (2), 1485–1494.
- (8) Murray, C. B.; Kagan, C. R.; Bawendi, M. G. Synthesis and Characterization of Monodisperse Nanocrystals and Close-Packed Nanocrystal Assemblies. *Annu. Rev. Mater. Sci.* **2000**, 30 (1), 545–610.
- (9) Chang, H.; Kim, B. H.; Jeong, H. Y.; Moon, J. H.; Park, M.; Shin, K.; Chae, S. I.; Lee, J.; Kang, T.; Choi, B. K.; Yang, J.; Bootharaju, M. S.; Song, H.; An, S. H.; Park, K. M.; Oh, J. Y.; Lee, H.; Kim, M. S.; Park, J.; Hyeon, T. Molecular-Level Understanding of Continuous Growth from Iron-Oxo Clusters to Iron Oxide Nanoparticles. *J. Am. Chem. Soc.* **2019**, *141* (17), 7037–7045.
- (10) Ito, D.; Yokoyama, S.; Zaikova, T.; Masuko, K.; Hutchison, J. E. Synthesis of ligand-stabilized metal oxide nanocrystals and epitaxial core/shell nanocrystals via a lower-temperature esterification process. *ACS Nano* **2014**, *8* (1), 64–75.
- (11) Plummer, L. K.; Hutchison, J. E. Understanding the Effects of Iron Precursor Ligation and Oxidation State Leads to Improved Synthetic Control for Spinel Iron Oxide Nanocrystals. *Inorg. Chem.* **2020**, *59* (20), 15074–15087.
- (12) Knecht, T. A.; Hutchison, J. E. Precursor and Surface Reactivities Influence the Early Growth of Indium Oxide Nanocrystals in a Reagent-Driven, Continuous Addition Synthesis. *Chem. Mater.* **2023**, 35 (8), 3151–3161.
- (13) Sanchez-Lievanos, K. R.; Stair, J. L.; Knowles, K. E. Cation Distribution in Spinel Ferrite Nanocrystals: Characterization, Impact on their Physical Properties, and Opportunities for Synthetic Control. *Inorg. Chem.* **2021**, *60* (7), 4291–4305.
- (14) Rost, C. M.; Sachet, E.; Borman, T.; Moballegh, A.; Dickey, E. C.; Hou, D.; Jones, J. L.; Curtarolo, S.; Maria, J.-P. Entropy-stabilized oxides. *Nat. Commun.* **2015**, *6* (1), 8485.
- (15) Kirkland, E. J.; Loane, R. F.; Silcox, J. Simulation of annular dark field stem images using a modified multislice method. *Ultramicroscopy* **1987**, 23 (1), 77–96.
- (16) Bard, A. J.; Faulkner, L. R.; White, H. S. Electrochemical Methods: Fundamentals and Applications; John Wiley & Sons, 2022.
- (17) Dey, G. R.; McCormick, C. R.; Soliman, S. S.; Darling, A. J.; Schaak, R. E. Chemical Insights into the Formation of Colloidal High Entropy Alloy Nanoparticles. *ACS Nano* **2023**, *17* (6), 5943–5955.

- (18) Shi, Y.; Xu, Q.; Tian, Z.; Liu, G.; Ma, C.; Zheng, W. Ionic liquid-hydroxide-mediated low-temperature synthesis of high-entropy perovskite oxide nanoparticles. *Nanoscale* **2022**, *14* (21), 7817–7827.
- (19) Deanhardt, M. L.; Stern, K. H. Solubility Products of Metal Oxides in Molten Salts by Coulometric Titration of Oxide Ion Through Zirconia Electrodes. J. Electrochem. Soc. 1981, 128 (12), 2577
- (20) Gregori, G.; Aerts, A.; Gladinez, K.; Rosseel, K.; Doneux, T.; Lim, J. Electrochemical measurement of solubility product of metal oxides in liquid metals by coulometric titration of oxygen. *Electrochim. Acta* 2022, 432, No. 141202.
- (21) Rönnback, R.; Salmi, T.; Vuori, A.; Haario, H.; Lehtonen, J.; Sundqvist, A.; Tirronen, E. Development of a kinetic model for the esterification of acetic acid with methanol in the presence of a homogeneous acid catalyst. *Chem. Eng. Sci.* **1997**, 52 (19), 3369–3381.
- (22) Shannon, R. D. Revised effective ionic radii and systematic studies of interatomic distances in halides and chalcogenides. *Acta Crystallogr., Sect. A* **1976**, 32 (5), 751–767.
- (23) Li, K.; Xue, D. Estimation of Electronegativity Values of Elements in Different Valence States. *J. Phys. Chem. A* **2006**, *110* (39), 11332–11337.